RESEARCH ARTICLE

NANO · MICRO small

www.small-journal.com

Tailoring C—N Containing Compounds into Carbon Nanomaterials with Tunable Morphologies for Electrocatalytic Applications

Wenchao Wan, Yonggui Zhao, Jie Meng, Christopher S. Allen, Ying Zhou,* and Greta R. Patzke**

Carbon materials with unique sp^2-hybridization are extensively researched for catalytic applications due to their excellent conductivity and tunable physicochemical properties. However, the development of economic approaches to tailoring carbon materials into desired morphologies remains a challenge. Herein, a convenient "bottom-up" strategy by pyrolysis of graphitic carbon nitride (g-C_3N_4) (or other carbon/nitrogen (C, N)-enriched compounds) together with selected metal salts and molecules is reported for the construction of different carbon-based catalysts with tunable morphologies, including carbon nano-balls, carbon nanotubes, nitrogen/sulfur (S, N) doped-carbon nanosheets, and single-atom catalysts, supported by carbon layers. The catalysts are systematically investigated through various microscopic, spectroscopic, and diffraction methods and they demonstrate promising and broad applications in electrocatalysis such as in the oxygen reduction reaction and water splitting. Mechanistic monitoring of the synthesis process through online thermogravimetric-gas chromatography-mass spectrometry measurements indicates that the release of C—N-related moieties, such as dicyan, plays a key role in the growth of carbon products. This enables to successfully predict other widely available precursor compounds beyond g-C_3N_4 such as caffeine, melamine, and urea. This work develops a novel and economic strategy to generate morphologically diverse carbon-based catalysts and provides new, essential insights into the growth mechanism of carbon nanomaterials syntheses.

1. Introduction

Carbon materials with abundant delocalized electrons due to their sp^2-hybridization have been extensively studied for electrocatalytic applications such as the oxygen reduction reaction (ORR) and water splitting.[1–3] However, conventional carbon materials, such as graphene and carbon nanotubes (CNTs), with uniform lattice structures are chemically inactive for catalytic reactions due to their weak adsorption of reactants.[4,5] To overcome this drawback, the creation of catalytically active sites on perfect carbon structures has become a crucial research branch in carbon-based catalysis.[6] To date, three strategies have been widely reported to activate carbon surfaces: first, coupling of materials with catalytically active components, such as metals and oxides,[7,8] second, replacing carbon atoms with a moderate amount of defects or dopants, such as N and S atoms,[9–13] and third, atomic dispersion of metal species on carbon to achieve highly exposed metal active sites.[14–21] All these synthetic strategies are based on two generally accepted rules: a) highly conductive carbon can efficiently

---

W. Wan, Y. Zhao, G. R. Patzke
Department of Chemistry
University of Zurich
Winterthurerstrasse 190, Zurich CH-8057, Switzerland
E-mail: wenchao.wan@cec.mpg.de; greta.patzke@chem.uzh.ch

W. Wan
Department of Heterogeneous Reactions
Max Planck Institute for Chemical Energy Conversion
D-45470 Mülheim an der Ruhr, Germany

The ORCID identification number(s) for the author(s) of this article can be found under https://doi.org/10.1002/smll.202304663

DOI: 10.1002/smll.202304663

J. Meng
Division of Chemical Physics
Lund University
Box 124, Lund 22100, Sweden

C. S. Allen
Electron Physical Science Imaging Center
Diamond Light Source Ltd
Didcot, Oxfordshire OX11 0DE, UK

C. S. Allen
Department of Materials
University of Oxford
Oxford OX1 3HP, UK

Y. Zhou
State Key Laboratory of Oil and Gas Reservoir Geology and Exploitation
Southwest Petroleum University
Chengdu 610500, China
E-mail: yzhou@swpu.edu.cn

promote electron transfer from catalysts to the electrodes to boost the redox cycles;[22] b) replacement of carbon atoms with moderate defects or heteroatom-dopants can significantly modify the electronic structure of the carbon lattice, thus optimizing the chemisorption of reactants.[4,23] The biggest advantage of these "carbon to catalyst" synthetic strategies using well-prepared carbon sources, such as graphene or CNT, is that the conductive nature of carbon in the final products can be well preserved through this moderate modification approach. This kind of approach, however, involves two chemical steps, namely carbon growth and carbon activation, which are extremely costly and time-consuming.[24,25]

Recently, the one-pot pyrolysis of C/N-containing complexes to grow carbon-based catalysts has received increasing attention due to the very simple synthetic procedure.[26–28] In particular, carbon-based catalysts with abundant metal active sites derived from metal-organic frameworks (MOFs) and their derivatives have become one of the most promising materials classes and have been successfully applied for a wide range of electrochemical energy conversion processes.[28,29] In a typical MOF structure, metal sites are well-coordinated to their non-metal ligands, which can efficiently suppress the aggregation of metal atoms during the pyrolysis, thus leading to the formation of highly dispersed metal species such as particles, clusters, or even single-atom catalysts (SACs).[30] In addition, the pyrolysis of Zn-based MOFs can directly generate metal-free N-doped carbon materials due to the evaporation of Zn metal.[31] However, the synthesis of MOFs as precursors on a large scale remains challenging due to their multi-step synthetic procedures and low yields.[32] Additionally, the pyrolysis of MOFs is a "top-down" strategy. As a consequence, the morphologies of the final products substantially depend on the initial morphological features of the MOFs,[33] which leaves little room for the following morphological regulation of carbon materials during pyrolysis. On the other hand, current studies on the pyrolysis process of MOFs and other precursors using a real-time technique to investigate the growth mechanisms of carbon products remain to be conducted. This need for mechanistic insight has limited the morphological design of carbon products as well as the exploration of other cheaper and sustainable precursors to scale up the synthesis of carbon-based catalysts.

In the present work, we introduce a "bottom-up" strategy using g-C_3N_4 (or other C/N-containing precursors) and a series of specific molecules as precursors to successfully fabricate a series of carbon materials with tunable 0D, 1D, and 2D morphologies. g-C_3N_4 can be produced on a large scale via one-step pyrolysis of dicyandiamide in the air, and it can be further replaced by other commercial compounds, such as melamine, urea, and caffeine, which renders this approach very promising for scaling up.[34]

Specifically, the use of glucose molecules reacting with g-C_3N_4 generates N-doped layered carbon materials, and with an extra sulfur source, (S, N)-co-doped carbon materials can be obtained as well. Metal phthalocyanine molecules and g-C_3N_4 as precursors give rise to the formation of carbon-supported SACs. Furthermore, mixtures of metal salts and g-C_3N_4 as precursors promote the growth of CNTs or carbon nano-balls. The structures and morphologies of the above carbon materials were characterized by X-ray diffraction (XRD), Raman spectroscopy, high-angle annular dark-field scanning transmission electron microscopy (HAADF-STEM), and X-ray absorption spectroscopy (XAS). They demonstrate promising electrocatalytic performance, such as in the oxygen evolution reaction (OER), the hydrogen evolution reaction (HER), and the ORR. In particular, (N, S)-co-doped carbon and carbon-supported Fe-SAC show impressive ORR performance, while CNTs and carbon ball-based catalysts display excellent OER and HER performances. Most importantly, for the first time, we investigated the pyrolysis process and the formation mechanism through online thermogravimetric-gas chromatography-mass spectrometry (TG-GC-MS) measurements. We revealed that the generation of hydrogen isocyanate and dicyan fragments that contain C/N moieties play key roles in the formation of the above carbon materials. Based on these mechanistic studies, other molecules with similar C/N-containing structures have been successfully predicted as precursors for the fabrication of the above-mentioned carbon materials. This provides a novel and flexible strategy for the synthesis of carbon materials with desired morphologies and offers a profound understanding of the growth mechanism of carbon materials through pyrolysis routes.

2. Results and Discussion

2.1. Syntheses and Structural Characterizations

The syntheses of the carbon materials with different dimensions follow a similar protocol, in which g-C_3N_4 powder and specific small molecules (glucose, phthalocyanine) and metal salts are physically mixed in certain solvents and subsequently subjected to a pyrolysis process (**Figure 1**). The detailed syntheses are described in the Supporting Information. Four types of carbon materials with specific morphologies were obtained after the pyrolysis of three different mixtures. When mixing g-C_3N_4 and glucose, an N-doped layered carbon material with 2D morphology was produced. Further introduction of sulfur as an additional element into the synthesis leads to the formation of (S, N)-co-doped carbon. When glucose was replaced with Ni-, Co-, or Fe-phthalocyanine molecules, 2D layered carbon-supported single Ni, Co, and Fe metal atom catalysts were fabricated (referred to as Ni/Co/Fe-SACs). Except for the 2D carbon materials, 1D CNTs and 0D carbon balls can be also achieved by pyrolysis of a mixture of g-C_3N_4 and Ni^{2+}, Co^{2+}, and Fe^{3+} ions with considerable amounts of metal nanoparticles inside (referred to as Ni/Co/Fe-CN).

N-doped carbon and (S, N)-co-doped carbon were investigated through transmission electron microscopy (TEM) and both displayed 2D morphological features. Carbon layers are randomly cross-linked and wrinkled together (**Figure 2**a–c and Figures S1 and S2, Supporting Information). On the edges of the carbon nanosheets, typical layered morphologies are present for both compound types (Figure 2c and Figure S2, Supporting Information). X-ray photoelectron spectra (XPS) (Figure 2d–f and Figures S3–S5, Supporting Information) indicate that the carbon-based layers are composed of carbon, nitrogen, oxygen, and sulfur (for

---

Y. Zhou
Institute of Carbon Neutrality & School of New Energy and Materials
Southwest Petroleum University
Chengdu 610500, China

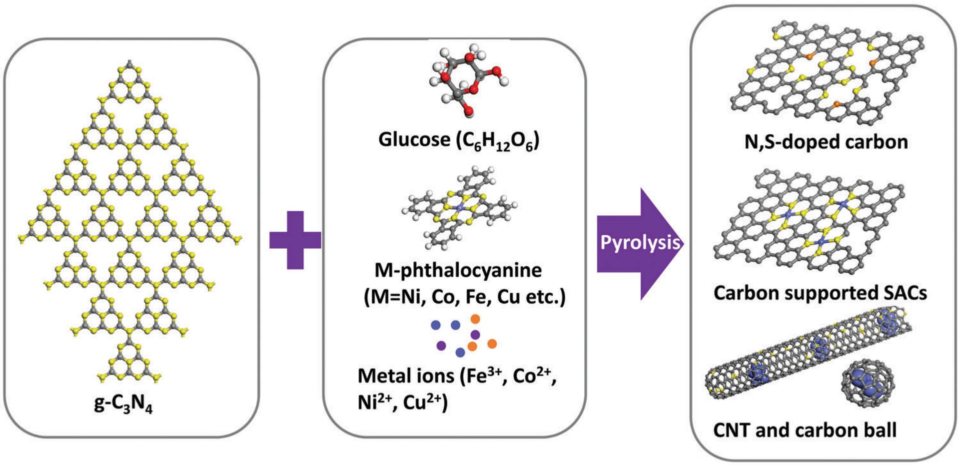

Figure 1. Synthetic scheme of (N, S)-co-doped carbon sheets, carbon-supported single-atoms, CNT, and carbon nano-ball wrapped metal nanoparticles.

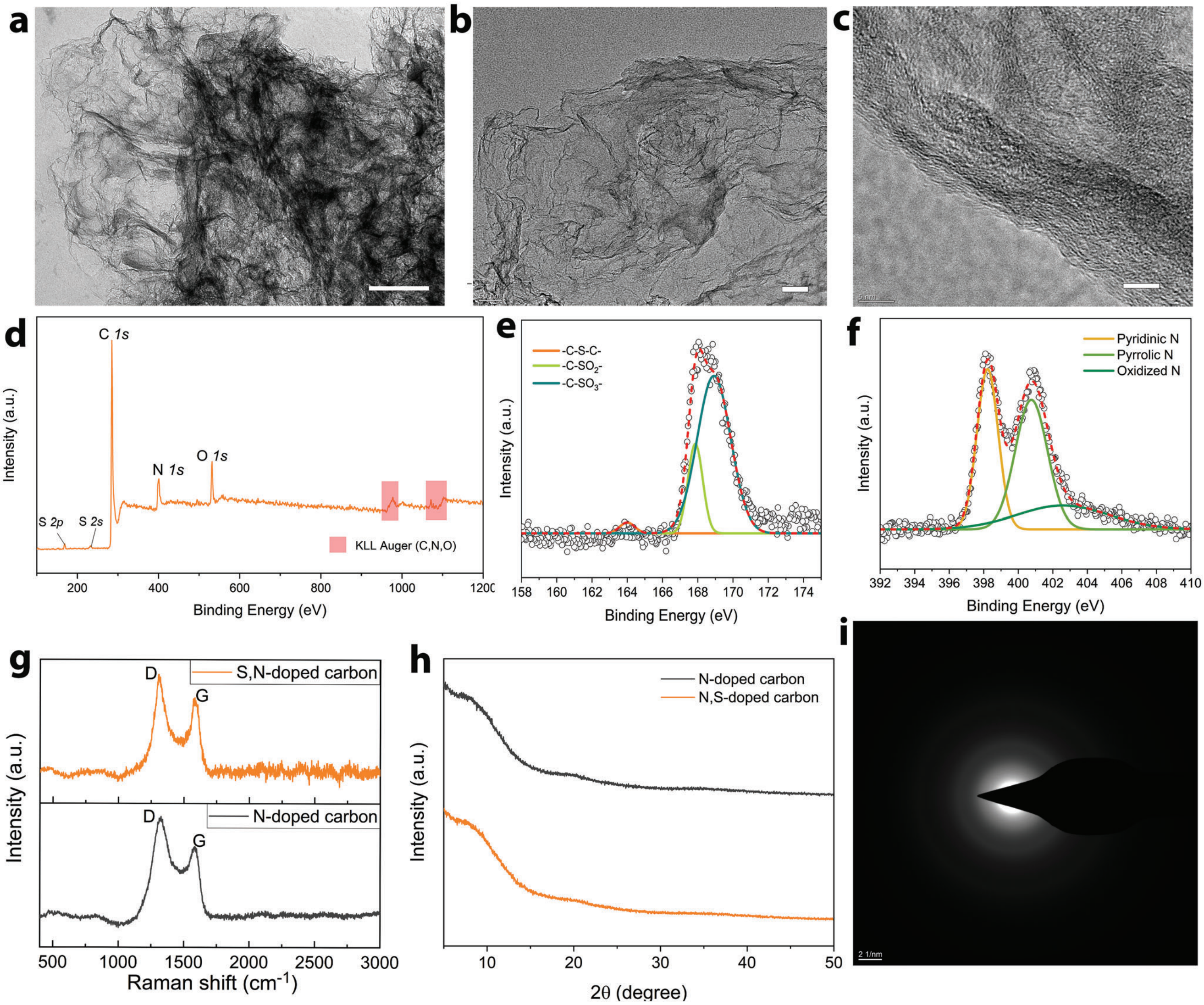

Figure 2. a–c) TEM images of (S, N)-co-doped carbon synthesized from g-C_3N_4 (scale bars = 200, 50, and 5 nm, respectively). d) XP survey spectrum. e,f) S 2p and N 1s high-resolution XP spectra of (S, N)-co-doped carbon. g,h) Raman spectra and PXRD patterns of N-doped and (S, N)-co-doped carbon. i) SAED pattern of (S, N)-co-doped carbon prepared at 1000 °C.

(S, N)-co-doped carbon). The presence of N suggests that structure motifs of g-C_3N_4 are partially preserved during pyrolysis. The deconvolution analyses of the high-resolution N 1s spectra of N and (S, N)-co-doped carbon materials show that the envelopes are dominated by two major peaks centered at 398.3 and 401 eV, which can be ascribed to pyridine- and pyrrole-like nitrogen, respectively (Figure 2f and Figure S4, Supporting Information). The weak peak around 403.5 eV can be assigned to the oxidized N species. Two S peaks positioned at 164 and 168.5 eV are observed in the S 2p high-resolution spectrum of (S, N)-co-doped carbon, which can be assigned to "C—S—C" and "C—SO_x ($x = 2$, 3)" bonds, respectively, based on the deconvolution of the peaks (Figure 2e).[35] The fitting of the C 1s demonstrates that sp^2 and sp^3 carbon structures are the main components. The presence of C—O/N and C═O peaks (Figures S4 and S5, Supporting Information) indicates that oxygen functional groups remain, which is also evident from the O 1s spectra. Raman spectra of N and (S, N)-co-doped carbon contain two typical D and G bands centered at 1350 and 1620 cm^{-1}, respectively, which have been widely reported for graphene-like materials (Figure 2g).[36] However, the absence of crystalline signals in the powder X-ray diffraction (PXRD) together with the blurry pattern of the selected area electron diffraction (SAED) measurement suggests the amorphous or defective nature of the carbon materials (Figure 2h,i).[37,38]

Carbon-supported SACs were prepared using metal phthalocyanine (metals = Ni, Co, and Fe) and g-C_3N_4 as the precursors. Metal phthalocyanine molecules were selected for the following two reasons: first, phthalocyanine molecules contain isolated metal centers with well-defined M-N_4 coordination which have been widely considered as the real active sites in carbon-supported SACs;[39–41] second, the phthalocyanine ligand contains carbon atoms with sp^2 hybridization, which serve as the basic unit for the polymerization of larger carbon layers together with the decomposition of g-C_3N_4. Conventional TEM images reveal that the obtained materials are composed of large-area carbon nanosheets with a random distribution, which is similar to the above-discussed N-doped carbon (Figures S6–S8, Supporting Information). It is worth mentioning that no obvious nanoparticles were observed during the TEM measurements. This is also evident from PXRD patterns and Raman spectra, wherein only carbon signals were detected (Figures S9 and S10, Supporting Information). To further identify the structure of the metal species, HAADF-STEM measurements were performed in which due to the power law dependence of HAADF-STEM intensity on atomic number, heavier atomic species appear brighter. Atomically resolved Ni, Co, and Fe atoms are imaged as discrete bright dots on the carbon substrate (**Figure 3**a–c). More STEM images at different magnifications and in different areas were acquired in both dark and bright-field STEM modes shown in Figures S11–S16, Supporting Information. The compositions of the materials were further determined by XPS and energy-dispersive X-ray spectroscopy (EDX) (Figures S17–S28, Supporting Information). Except for the metals, the materials also contain N, C, and O. The EDX mapping results reveal that the average metal contents of Ni-SAC, Co-SAC, and Fe-SAC are 5.26, 7.5, and 4.8 wt%, respectively (Figures S20–S28, Supporting Information). The metal contents in the bulk were also determined by inductively coupled plasma triple quadrupole mass spectrometry (ICP-MS), as 9.5, 12.4, and 10.6 wt%, respectively. These determined metal contents are higher than most of the current reported carbon-supported SACs.[42,43] The oxidation states of the metal species were further identified by XPS (Figures S17–S19, Supporting Information). The deconvolution analyses of the high-resolution Ni 2p spectrum of Ni-SAC are dominated by a rather narrow spin-orbit doublet with Ni $2p_{3/2}$ core level at 855.2 eV, suggesting a diamagnetic feature of the Ni species and an oxidation state of Ni^{2+}. In contrast to Ni-SAC, Co 2p and Fe 2p spectra of Co-SAC and Fe-SAC contain rather broader 3/2 core levels at 780.8 and 710.3 eV, respectively, and show significant satellite features, indicating the paramagnetic character of Co^{2+} and Fe^{3+} species.[44] The analyses of N 1s and O 1s spectra show that pyridinic and pyrrolic N are the main N species, while sp^2, sp^3, and C—O/N species are dominant in the carbon signal (Figures S17–S19, Supporting Information).

To further investigate the local structure and oxidation states of the metal species supported on the carbon matrix, metal K-edge XAS experiments were performed. As illustrated in Figure 3d, the presence of a pre-edge peak at 7112.5 eV in the XANES spectrum of Fe-SAC can be assigned to the 1s to 3d transition, which is dipole-forbidden but quadrupole allowed by the mixing between metallic d- and ligand p-orbitals.[45] The pre-edge feature is very similar to the FePc reference (oxidized in air) and usually indicates unfilled d-orbitals so that the Fe species in Fe-SAC contain Fe^{3+}. However, the shape and position of the pre-edge peak were slightly changed in comparison to FePc, indicating the oxidation or changes in the coordination environment of the Fe centers. There are two possible reasons for the absence of the 1s to $4p_z$ transition in Fe-SAC: i) the adsorption of O_2 or H_2O molecules can lead to distortion of the D_{4h} symmetry; ii) partial oxidation of the Fe species to form a μ-oxo derivative of square-pyramidal symmetry.[46,47] The rising edge of Fe-SAC is located between FeO and Fe_2O_3, but approaching that of Fe_2O_3 at a higher energy range, indicating a main oxidation state of +3. The XANES of Co-SAC (Figure 3e) shows similar results: the increase of the pre-edge peak and the disappearance of the 1s to $4p_z$ transition compared to CoPc suggest distortion or oxidation of the Co centers after pyrolysis. The overlapping of the rising edge with that of CoO indicates the dominance of Co^{2+} species in Co-SAC. In contrast to Fe-SAC and Co-SAC, a slight decrease in the 1s to $4p_z$ transition and an enhancement in the 1s to 3d transition are observed in Ni-SAC (Figure 3f), suggesting that the D_{4h} symmetry is still preserved in the material. The overlapping of the rising edge with those of NiPc and NiO suggests that the overall oxidation state of Ni species is Ni^{2+}. Combining both the XANES and XPS results, it is safe to conclude that Ni^{2+}, Co^{2+}, and Fe^{3+} are the main species in Ni-SAC, Co-SAC, and Fe-SAC, respectively.

The local structures were determined from Fourier-transform extended X-ray absorption fine structure (FT-EXAFS) spectra (Figure 3g–i), in which similar backscattering features at 1.4–1.45 Å are present for all samples. Considering that the position of this signal overlaps with those of M-N paths in Ni-, Co-, and Fe-phthalocyanine molecules (Figure 3g–i) and that the STEM images of the SACs clearly show atomic dispersion of the metal, it is reasonable to assume that the isolated features of metal sites in the phthalocyanine molecules are still preserved after pyrolysis. Therefore, the first coordination shell can be assigned to M-N paths. However, vertical "out-of-plane" M-O coordination may also exist as has been discussed in the section on XANES, but currently, XAS cannot distinguish the M-N and M-O paths. It is

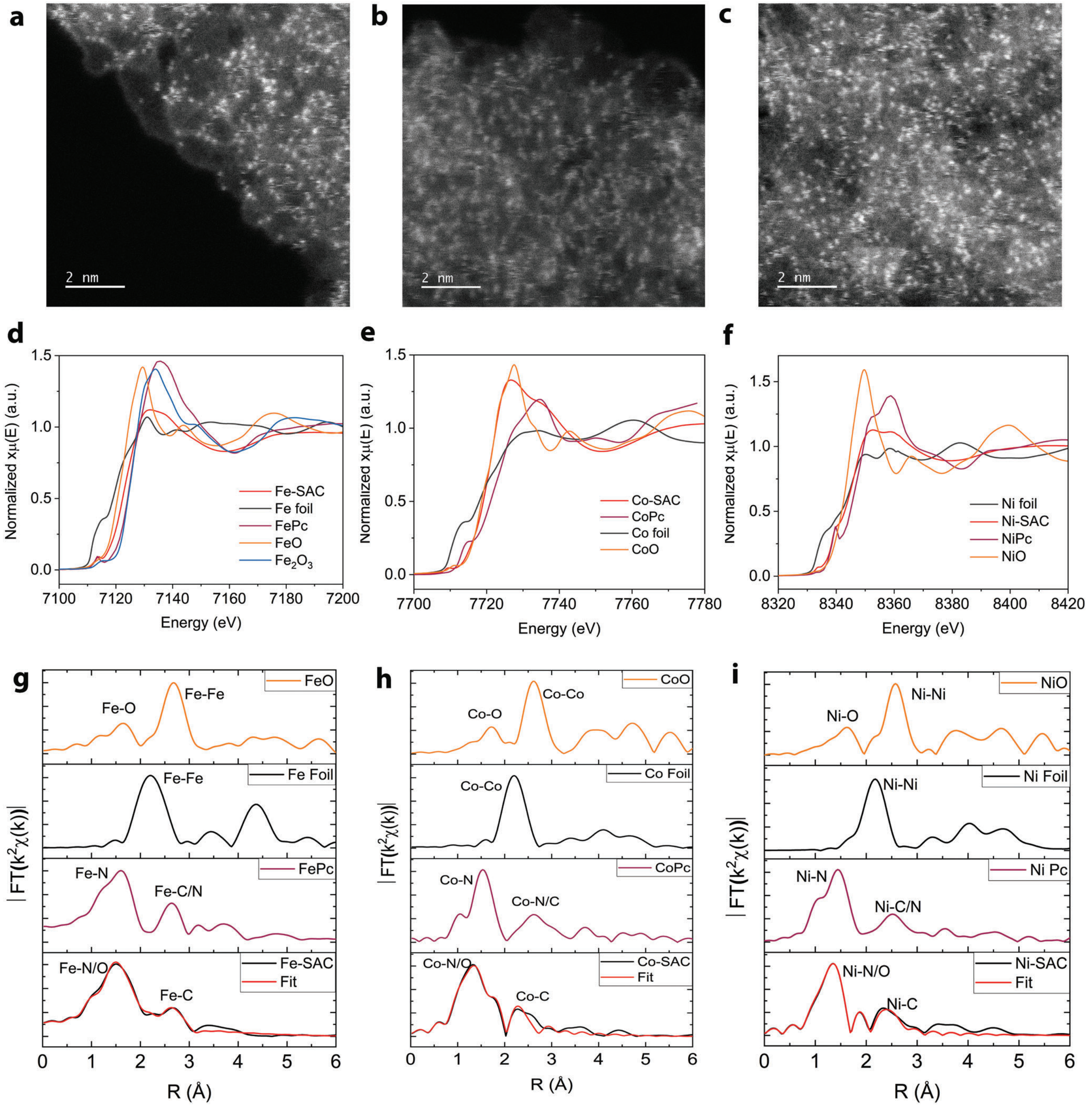

Figure 3. a–c) HAADF-STEM images of carbon-supported single a) Ni, b) Co, and c) Fe atoms at different magnifications. d–f) K-edge XANES spectra and g–i) Fourier transform *K*-edge EXAFS spectra of Fe-SAC, Co-SAC, and Ni-SAC, along with reference samples.

worth noting that a shoulder peak between 2 and 3 Å is present in all of the samples. The position is very close to the M-M path in their foil references but also overlaps with the M-C/N paths in MPc references. To shed more light on this issue, the comparison of the wavelet transforms of the k^2-weighted EXAFS signals to their corresponding metal foil references was performed (Figure S29d–f, Supporting Information). The results show that the scattering signal between 2 and 3 Å is not as strong as for the foil references, which indicates that these backscattering signals are from non-metal absorbers. This is also evident from the comparison of their *K* spaces. The multiple scattering of M-M in foils is around 6–8 $Å^{-1}$, however, at the same position, the scattering feature in the SACs is completely different (Figure S29a–c, Supporting Information). Based on the above analyses, the M-C path in the second coordination sphere was implemented in the fitting analysis, and the results fit quite well with the

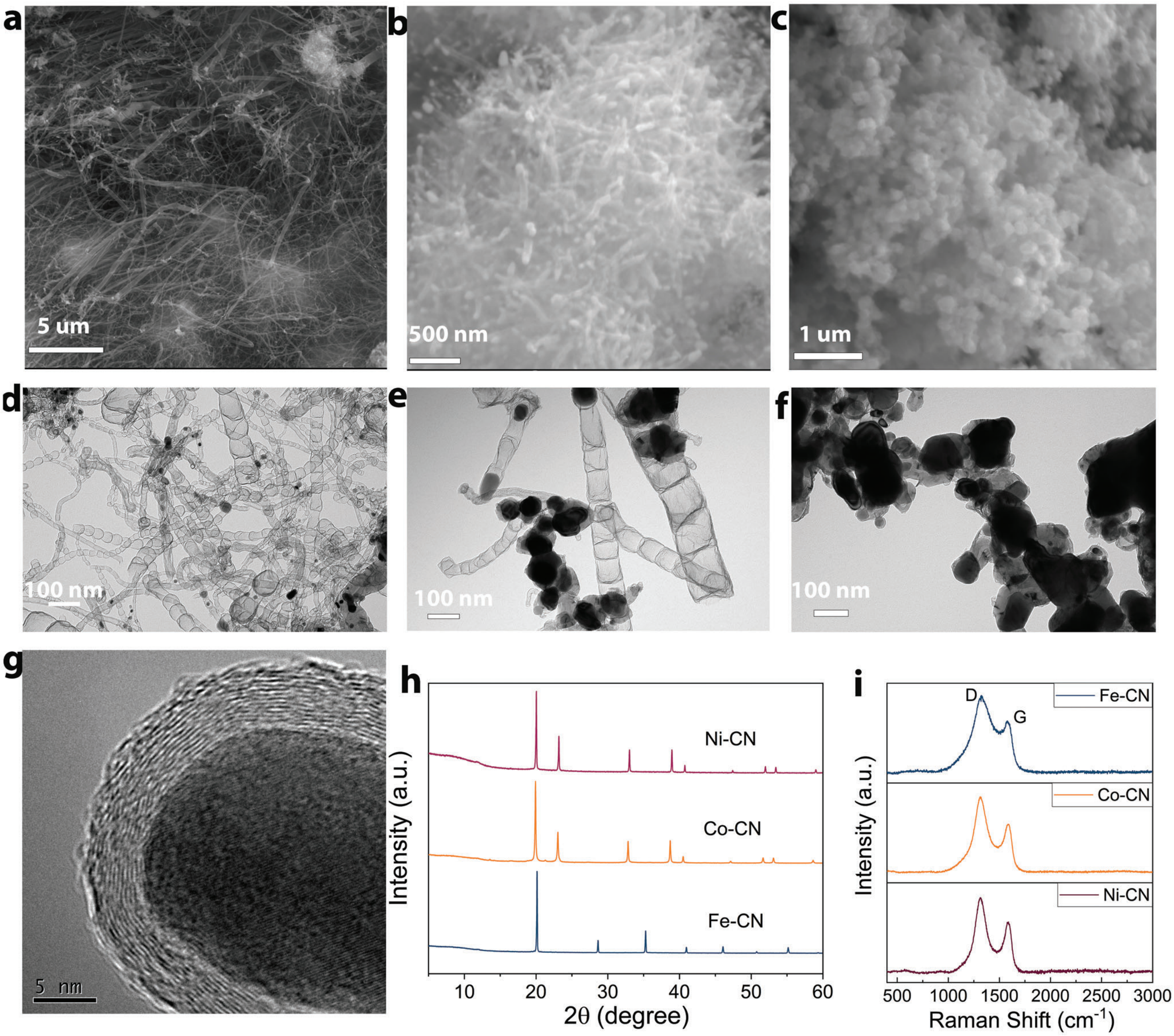

Figure 4. a–c) SEM and d–f) TEM images of Ni-CN, Co-CN, and Fe-CN. g) HRTEM image of NiFe-CN. h) PXRD patterns and i) Raman spectra of the samples.

experimental data (Figures S30–S35 and Table S1, Supporting Information). Nevertheless, it is still arbitrary to exclude the existence of minor amounts of clusters or particles since the XAS analysis is a statistical method, and STEM analysis only provides insight into limited areas of the materials. However, when combining all these results of XAS, STEM images, and XPS, it is convincing to conclude that the majority of the metal species on the carbon should be atomically dispersed metal atoms.

CNT and metal nanoparticles encapsulated into carbon balls were obtained through pyrolysis of different 3d transition metal ions, including Ni^{2+}, Co^{2+}, and Fe^{3+}, together with $g\text{-}C_3N_4$. Scanning electron microscope (SEM) and TEM images reveal that the morphologies of the carbon products vary with the use of different 3d metals (**Figure 4**a–f and Figures S36–S41, Supporting Information). The presence of Ni^{2+} resulted in the formation of CNTs (Figures S36–S37, Supporting Information), while Fe^{3+} gives rise to the formation of ball-like carbon particles (Figures S40 and S41, Supporting Information). Carbon products obtained in the presence of Co^{2+} contain both CNTs and carbon balls (Figure 4b and Figures S38 and S39, Supporting Information). However, all the above materials show the same morphological features with metal nanoparticles encapsulated inside the carbon matrix. Raman spectra display typical D and G bands at around 1350 and 1580 cm^{-1}, respectively, for all samples, which are characteristic of graphene-like materials and indicate this structure of the materials (Figure 4i).[48,49] In the PXRD patterns, only the characteristic peaks of Ni, Co, and Fe metals were observed, suggesting the presence of metallic NPs in these materials (Figure 4h). In addition to the single metal centers, NiFe and CoFe alloys encapsulated into carbon were also synthesized as

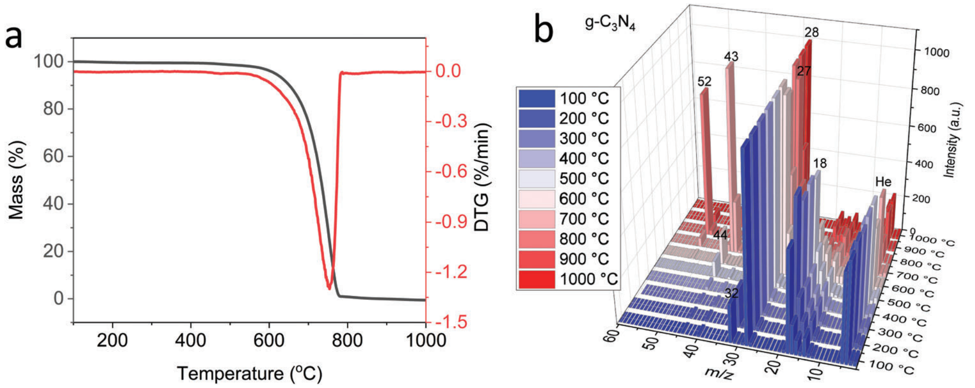

Figure 5. a) TG and DTG spectra of g-C_3N_4. b) Mass spectra of g-C_3N_4 measured with TG-GC-MS.

shown in Figures S42 and S43, Supporting Information. TEM images show that CNTs were formed in all samples and the HRTEM images of NiFe-CN clearly show that the NPs are well-wrapped into the carbon layers (Figure 4g). However, during syntheses, we found that only the presence of Ni or Co metal can successfully promote the formation of CNTs. This implies that the resulting morphologies are highly correlated to the nature of the 3d metal. This result is discussed in the following section.

2.2. Formation Mechanism

To investigate the role of g-C_3N_4 and other precursors in the formation mechanism, online TG-GC-MS measurements were performed. It is noteworthy that TG-GC-MS is a synergetic analysis, wherein the products formed during the synthesis can be successively separated and analyzed by TG, GC, and MS (for experimental details please consult the Supporting Information).

The TG analysis of bare g-C_3N_4 shows that its decomposition starts at around 600 °C and is completed at around 750 °C (**Figure 5**a). The decomposition process was further analyzed by TG-GC-MS. Six main radicals with masses of 18, 27, 28, 43, 44, and 52 were observed (Figure 5b). According to the initial structure of g-C_3N_4 as well as in line with database information of TG-GC-MS, these masses can be assigned to H_2O, hydrogen cyanide, CO, hydrogen isocyanate, CO_2, and dicyan, respectively. The generation of oxygen-containing molecules including CO and CO_2 may arise from the reaction between the oxygen-related functional groups and the g-C_3N_4 structure. The hydrogen-related species, such as hydrogen cyanide and hydrogen isocyanate, are likely to be generated from the reaction between dicyan and oxygen or hydrogen-containing groups. These may potentially arise from the synthesis of g-C_3N_4 since the precursor dicyandiamide contains abundant hydrogen groups and the entire synthesis was performed in air.[50] Interestingly, the structural motifs of all these C/N-containing species, namely hydrogen cyanide, hydrogen isocyanate, and dicyan, can be found in the original structure of g-C_3N_4 (**Figure 6**a), implying that the C/N-containing species may provide the actual carbon and nitrogen sources for the growth of these three types of carbon materials. Based on the analyses of both TG and mass spectra, the whole decomposition process of g-C_3N_4 can be divided into three parts. First, H_2O ($M = 18$) and CO ($M = 28$) are released at around 100 °C, and this release went on during the whole process. Then CO_2 ($M = 44$) release set in above 500 °C. Finally, the C/N components appeared subsequently when the temperature was raised above 600 °C. It is worth noting that the masses of 17 and 16 were observed in all measurements and their relative intensities in the mass spectra were highly correlated to H_2O ($M = 18$). Therefore, it is reasonable to assign them to oxygen-related groups such as —OH and —O. Other signals, such as mass 32, with a weaker intensity than helium (carrier gas) may arise from impurities in the carrier gas since their intensities remain the same.

Based on the above information, we first studied the formation process of N-doped carbon. TG analysis shows that g-C_3N_4 and glucose follow two completely different decomposition processes (Figure S44, Supporting Information). Interestingly, the decomposition of the mixture of glucose and g-C_3N_4 at around 330 °C was absent in the TG spectrum, which suggests that the interaction between glucose and g-C_3N_4 in the mixture leads to different chemical reactions during the pyrolysis process. Mass spectra demonstrate that the decomposition of glucose only produced H_2O, CO, and CO_2. Hydrogen cyanide, hydrogen isocyanate, and dicyan were only observed in the precursors containing g-C_3N_4. Importantly, the intensity of the dicyan peak ($M = 52$) was significantly suppressed in the mixture compared to bare g-C_3N_4, indicating that dicyan was partially preserved within the final product after pyrolysis (Figure S45, Supporting Information). It is worth mentioning that even though only 10 wt% of g-C_3N_4 was replaced by glucose in the mixture, the intensity loss of the dicyan signal is up to 70%. Considering that all the measurements used similar amounts of starting materials, the depression of the dicyan signal in the mass spectra should not be due to a deficit of g-C_3N_4. This is also evident from the XPS results, in which pyridine- and pyrrole-like nitrogen centers were observed (Figure S4, Supporting Information). Based on the above discussion, the formation of N-doped carbon can be attributed to the reaction between dicyan and glucose, in which dicyan species provide the N dopant and chemically react with carbon during pyrolysis to form pyridine- and pyrrole-like nitrogen (Figure 6b).

The decomposition of g-C_3N_4 and metal phthalocyanines to form SACs displays a very similar result when compared to bare g-C_3N_4 regarding the TG and DTG spectra (Figure S46, Supporting Information). However, mass spectra show significant differences compared with bare g-C_3N_4 (Figure S47, Supporting Information). First, the signal of hydrogen isocyanate ($M = 43$) is

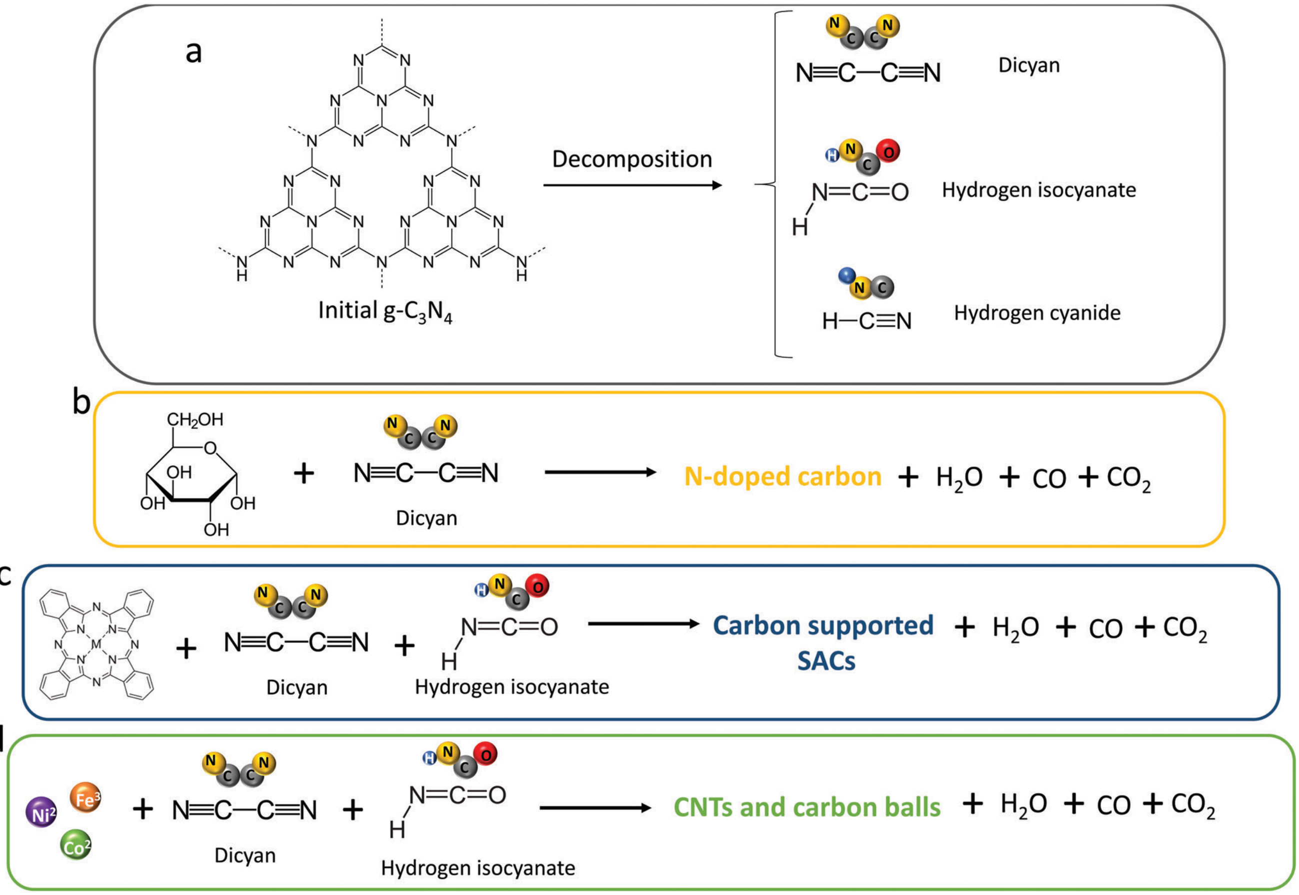

Figure 6. a) Products of the decomposition of g-C_3N_4. b–d) Possible reactions that occur to form N-doped carbon, carbon-supported SACs, CNTs, and carbon balls.

completely absent in the mixtures during the whole pyrolysis process. Second, the release of dicyan (M = 52) is dramatically reduced in the mixtures. As mentioned in the above section, the decrease of the dicyan signal caused by loss of g-C_3N_4 can be excluded since the content of phthalocyanine molecules in the precursor is only 10 wt% (see the experimental section in the Supporting Information), which is far less than what would account for the loss of the dicyan signal. Therefore, hydrogen isocyanate and dicyan are likely to be the reactants to form the final SACs with MPc molecules. Interestingly, the mass spectra of bare NiPc only show CO (M = 28) and H_2O (M = 18) signals during the entire decomposition process, implying that the structure was decomposed due to the adsorbed O_2 or H_2O and that the N-related structure is well preserved. This may further explain the atomic dispersion of metal atoms on carbon, where the nitrogen coordination around the metal sites in the MPc molecules is not completely affected. With all this information at hand, the SAC formation process can be considered as the result of reactions between hydrogen isocyanate, dicyan, and MPcs, where MPcs are partially decomposed and further connected to C/N containing structures such as dicyan (Figure 6c).

The growth of CNTs has been widely reported in previous works.[51,52] Usually the (111) crystal facet in Ni, Co, and Fe metal is the catalytically most active plane for the growth of CNTs.[53] This may explain the phenomenon that CNTs are only formed in Ni-CN and Co-CN in our experiment since they are dominated by the (111) crystal facet in their PXRD patterns, while the main crystal facet for Fe is (110) (Figure 4k). However, the formation of CNTs was not observed in Co-CN at the beginning when evaporation was used to remove the water in the synthesis, although the (111) crystal facet is the dominant reflection in the PXRD pattern (Figure S48a,b, Supporting Information). We suspect that the size of the metal NPs may also play a crucial role in the growth of CNTs, which has been observed in our previous work and in other studies.[54,55] To verify our hypothesis, the freeze-drying strategy was employed to reduce the particle size of Co instead of evaporation to remove water during the synthesis. As expected, notable amounts of CNTs were observed in the sample (Figure S48c,d, Supporting Information). To shed more light on the influence of particle size on the growth, a ligand confinement strategy was further applied to control the size of the metal particles. Ni-containing molecules with different ligands, including acetate and acetylacetone, were selected since Ni is the best candidate for the growth of CNTs in our case. SEM images show that the morphologies of CNTs are quite diverse (Figures S49–S51, Supporting Information). The CNTs prepared with nickel acetate are more uniform compared to those which were prepared with nickel nitrate, and the average diameter of CNTs is

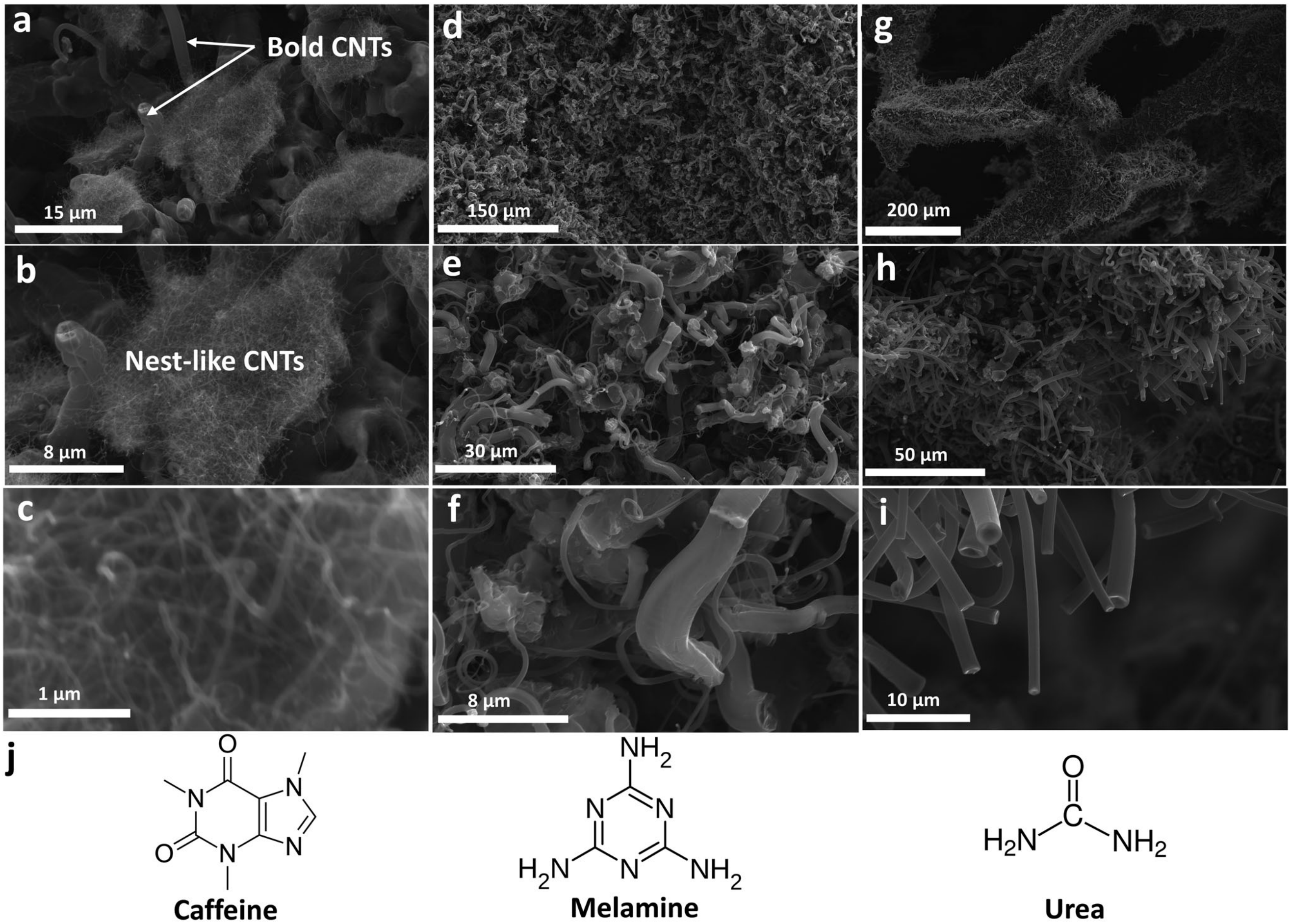

Figure 7. SEM images of CNTs grown on Ni foam using a–c) caffeine, d–f) melamine, and g–i) urea as precursors. j) Structures of caffeine, melamine, and urea.

about 50 nm as shown in Figure S49, Supporting Information. The overall diameter of the CNTs prepared with nickel acetylacetone is smaller compared to those prepared with nickel acetate with a range from 20 to 40 nm (Figure S50, Supporting Information). In contrast, the diameters of CNTs synthesized by nickel nitrate ranged from 30 to 100 nm (Figure S51, Supporting Information). In addition, the length of the CNTs synthesized by nickel acetylacetone is much longer compared to their counterparts emerging from nickel nitrate and nickel acetate. The above investigation indicates that the control of CNT growth regarding diameter and length via solid-state pyrolysis is possible, which may provide a guideline for future practical applications of this approach.

The TG plots of g-C$_3$N$_4$ combined with Ni/Co/Fe nitrates are similar to that of bare g-C$_3$N$_4$, suggesting that the main decomposition still arises from g-C$_3$N$_4$ (Figure S52, Supporting Information), which provides evidence that the carbon source for the growth of CNTs and carbon balls is the decomposition of g-C$_3$N$_4$. To understand the growth mechanism and the roles of the precursors, we designed a control experiment, where g-C$_3$N$_4$ powder and a piece of Ni foam were separately placed upstream and downstream in the furnace, respectively. As expected, CNTs were grown on the surface of Ni foam. This provides key evidence that the formation of metal NPs is a prerequisite for growing CNTs. SEM images clearly show that Ni NPs were present in the middle or at the tip of the CNTs (Figure S53, Supporting Information). It seems that "—C═N—" fragments from the decomposition of g-C$_3$N$_4$ were first captured by Ni foam and then reduced by the Ni NPs to form CNTs. Ni NPs were then dragged out from the surface and pushed away into the CNTs. This phenomenon agrees well with the mass spectra shown in Figure S54, Supporting Information, where the release of dicyan and hydrogen isocyanate was significantly and completely suppressed, respectively, indicating that they are converted into carbon at the surface. Based on the above studies, the growth mechanism can be described in three steps (Figure 5d and Figure S55, Supporting Information): first, C/N-containing species arising from g-C$_3$N$_4$ decomposition reach the surface of the foam with freshly exposed Ni NPs; then the C/N species react with Ni NPs to form carbon, and meanwhile, Ni NPs are encapsulated into CNTs. Finally, Ni NPs are further pushed away from the surface along with the growth of CNTs. It also seems that if there are no further metal NPs dragged from the surface, the growth process will spontaneously stop. This is also the reason why metal NPs are present not only at the top but also in the middle of CNTs.

2.3. Perspectives

Understanding the mechanisms of solid-state syntheses is extremely challenging due to the lack of detection options for the precise reactants released from the precursors. The current TG-GC-MS studies have revealed detailed decomposition processes of the precursors and provided abundant structural information on the actual reactants. The results suggest that the presence of "—C═N—" fragments in the precursor plays a crucial role in the formation of carbon materials. This information may provide an important clue to identifying more convenient molecules as substitutes for g-C_3N_4 to obtain the above three carbon materials. Therefore, it is reasonable to propose that other compounds that contain "—C═N—" units may also be used as the carbon source for producing carbon materials. To confirm our hypothesis, three very widely used compounds, namely caffeine, melamine, and urea, were selected as alternative precursors. As expected, all the selected compounds successfully generated CNTs as shown in the SEM images (**Figure 7**). However, the morphologies of the CNTs are very different. CNTs produced with caffeine display two morphologies: bold CNTs with a larger diameter and nest-like CNTs with a small diameter. CNTs prepared from melamine also display an irregular morphology and are randomly intertwined. Compared to caffeine and melamine, the morphology of CNTs fabricated via urea is quite uniform, and all CNTs are straight with similar diameters. The different morphologies of CNTs may correlate with the original structures of the precursors and their different diffusion behaviors during the pyrolysis process. N-doped carbon and carbon-supported SACs were also successfully prepared by using melamine as the precursor together with glucose and MPcs, respectively (Figures S56–S59, Supporting Information).

2.4. Electrochemical Applications

The reported materials with different morphologies show promise for electrocatalytic applications. N-doped and (S, N)-co-doped carbon materials display impressive ORR performances (**Figure 8**a,b). Particularly, N-doped carbon synthesized at 900 °C displays the best ORR catalytic performances with a half-wave potential of 0.82 V versus RHE and a limiting current density of 4.65 mA cm^{-2}. The best ORR performance for (S, N)-co-doped carbon was obtained for products synthesized at 900 °C. It shows a similar half-wave as for N-doped carbon (0.83 V vs RHE), however, the limiting current density (6.5 mA cm^{-2}) outperforms all of the other catalysts including the commercial Pt/C. The above results demonstrate that the ORR performances of the studied carbon materials are very sensitive to the pyrolysis temperature. This may correlate to the carbonization of carbon and the content of (S, N) dopants.[56,57] Higher pyrolysis temperatures lead to better conductivity of carbon compared to low temperatures (Figure S60, Supporting Information), which is usually favorable for electron transfer. However, high synthetic temperatures can also

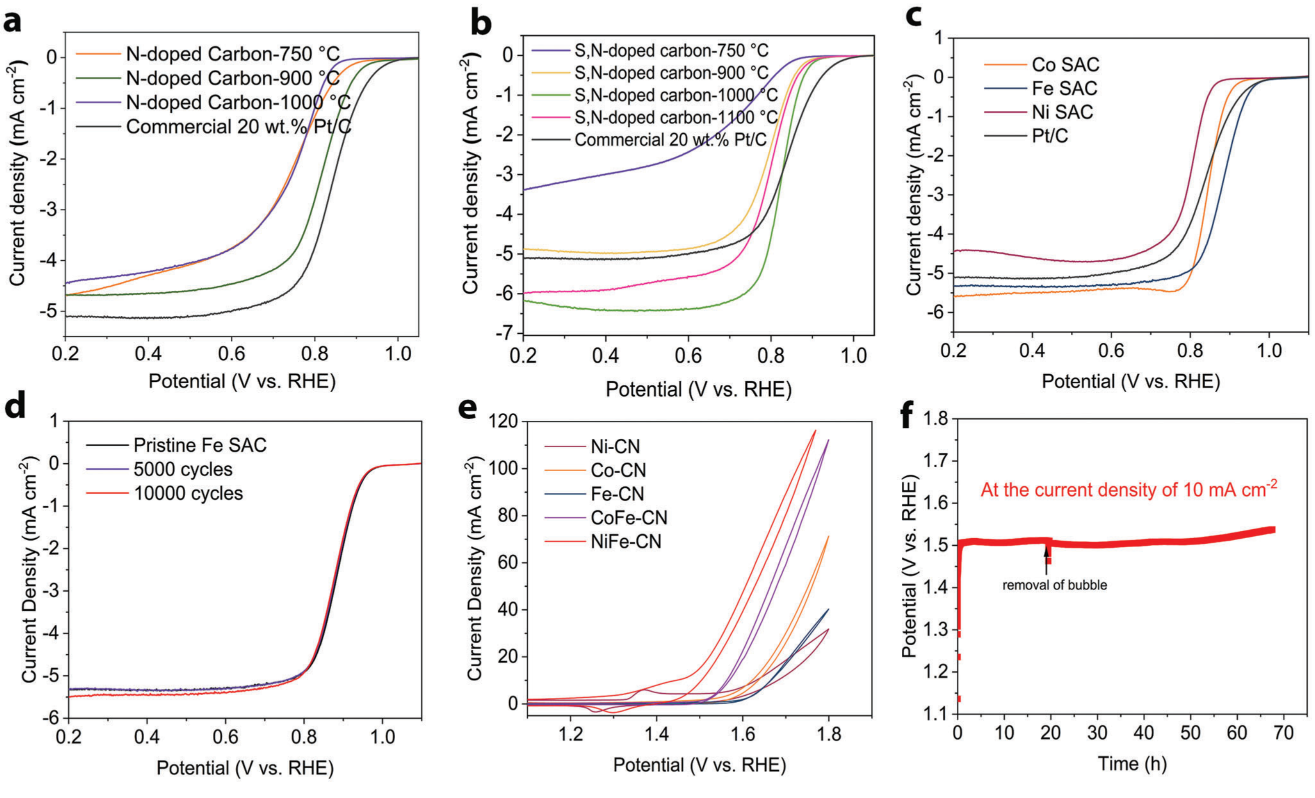

Figure 8. Electrochemical ORR and OER performances. ORR polarization curves of a) N-doped carbon, b) (S, N)-co-doped carbon, and c) Fe-, Co-, and Ni-SAC in O_2-saturated 0.1 м KOH at a scan rate of 5 mV s^{-1}. d) LSV curves of Fe-SAC after 5000 and 10 000 CV cycles. e) CV curves of Ni-CN, Co-CN, Fe-CN, CoFe-CN, and NiFe-CN for the OER. f) Stability test of NiFe-CN on carbon cloth at the current density of 10 mA cm^{-2}.

remove significant amounts of (S, N) dopants. It has been widely reported in previous works that a moderate content of N and S dopants in carbon materials can promote ORR performance.[58] This can explain why the best ORR performances of N-doped and (S, N)-co-doped carbon materials are not observed for the same synthesis temperature. The ORR kinetics of the N-doped and (S, N)-co-doped carbon materials were evaluated by rotating ring-disk electrode (RRDE) techniques (Figures S61 and S62, Supporting Information). The K–L plots show good linear and parallel characteristics, implying first-order reaction kinetics. The determined average numbers of electron transfer for N-doped and (S, N)-co-doped carbon materials are 3.8 and 4.15, respectively, which are very close to the four-electron transfer process of the ORR. The (S, N)-co-doped carbon synthesized at 1000 °C also shows good stability (Figure S63, Supporting Information). Carbon-supported SACs demonstrate more promising ORR performance. In particular, Fe- and Co-SAC exhibit impressive half-wave potentials of 0.88 and 0.84 V versus RHE, respectively, which are 20 and 60 mV higher than that of commercial Pt/C. The stability test of Fe-SAC shows a minor decline in both the half-wave potential and the limiting current density after 10 000 CV cycles (Figure 8d), and the current only decreases by 6 % after more than 24 h of chronoamperometry test at 0.5 V versus RHE. No obvious structural changes were observed based on the Raman, XAS, and TEM measurements after ORR. Except for the ORR, the carbon encapsulated series exhibits excellent OER performance as shown in Figure 8e. Among all the catalysts, NiFe-CN demonstrates the best OER activity with an overpotential of 290 mV versus RHE at the current density of 10 mA cm^{-2}. The stability test shows that the overpotential barely increased after around 70 h when holding the current density at 10 mA cm^{-2} (Figure 8f). The SEM images and Raman spectra remain unchanged after OER compared to the pristine sample, indicating that the morphology and structure are quite stable during the reaction. In addition to the OER, NiFe-CN also displays decent HER performance as shown in Figure S64a, Supporting Information, and can thus be further used in full-cell setups for overall water splitting. Only 0.9 V was applied in a two-electrode system to obtain the current density of 10 mA cm^{-2}, and the potential stays around 0.9 V without any increase even after 45 h (Figure S64b, Supporting Information).

3. Conclusion

We introduced a convenient molecular tailoring strategy to convert g-C_3N_4 into different carbon materials with controllable morphologies, namely (S, N)-co-doped carbon, SACs supported on layered carbon, CNTs, and metal nanoparticles encapsulated into carbon balls. Microscopic and spectroscopic characterizations were systematically applied to investigate their respective morphologies and structures. Importantly, for the first time, the formation processes were fundamentally investigated through the online TG-GC-MS and we found that the basic C/N-containing units in g-C_3N_4 are the key reactants for the growth of carbon materials. The interactions between the C/N-containing fragments and different precursors drive the formation of specific structures and morphologies. Our mechanistic study led to the successful prediction of other precursors for tailored carbon nanomaterials beyond g-C_3N_4 such as caffeine, melamine, and urea. Moreover, the reported carbon materials with specific morphologies were further evaluated for electrocatalytic ORR and OER applications. (S, N)-co-doped carbon and carbon-supported Fe SACs demonstrate impressive ORR performance. CNT-encapsulated NiFe alloy displays both excellent OER and HER activities.

This molecular tailoring strategy provides new and simple ways to tune the morphologies of carbon materials via solid-state pyrolysis for a wide range of catalytic applications. We show that not only the morphologies of the carbon materials but also the diameter and the length of CNTs can be chemically modulated through different precursor molecules. This provides facile opportunities to optimize carbon products for practical applications. On the other hand, the proposed solid-state strategy offers a very flexible way to functionalize carbon materials. For instance, the introduction of additional S dopants onto the carbon significantly promoted the ORR performance, and the alloying of Ni and Fe inside the carbon impressively boosted the OER performance. We expect that our application-oriented synthesis will provide future research strategies for carbon materials to rationally design and synthesize low-cost and highly-performing carbon-based catalysts.

Supporting Information

Supporting Information is available from the Wiley Online Library or from the author.

Acknowledgements

W.W. and Y.Z. contributed equally to this work. This research was supported by the University of Zurich Research Priority Program for Solar Light to Chemical Energy Conversion (URPP LightChEC). The authors thank the Diamond Light Source for access and support in the use of the electron Physical Science Imaging Centre (Instrument E02, proposal number MG23517) that contributed to the results presented here.

Open access funding provided by Universität Zürich.

Conflict of Interest

The authors declare no conflict of interest.

Data Availability Statement

The data that support the findings of this study are available from the corresponding author upon reasonable request.

Keywords

carbon nanotubes, carbon nitride, electrocatalysis, N-doped carbon, single-atom catalysts

Received: June 6, 2023
Revised: July 26, 2023
Published online: October 11, 2023

---

[1] X. Feng, Y. Bai, M. Liu, Y. Li, H. Yang, X. Wang, C. Wu, *Energy Environ. Sci.* **2021**, *14*, 2036.

[2] Y. Zhao, R. Nakamura, K. Kamiya, S. Nakanishi, K. Hashimoto, *Nat. Commun.* **2013**, *4*, 2390.
[3] Z. Lu, G. Chen, S. Siahrostami, Z. Chen, K. Liu, J. Xie, L. Liao, T. Wu, D. Lin, Y. Liu, T. F. Jaramillo, J. K. Nørskov, Y. Cui, *Nat. Catal.* **2018**, *1*, 156.
[4] J. Zhu, S. Mu, *Adv. Funct. Mater.* **2020**, *30*, 2001097.
[5] J. N. Tiwari, N. K. Dang, S. Sultan, P. Thangavel, H.u Y. Jeong, K. S. Kim, *Nat. Sustainability* **2020**, *3*, 556.
[6] L. Wang, D. Wang, Y. Li, *Carbon Energy* **2022**, *4*, 1021.
[7] L. He, F. Weniger, H. Neumann, M. Beller, *Angew. Chem., Int. Ed.* **2016**, *55*, 12582.
[8] J. Hwang, A. Ejsmont, R. Freund, J. Goscianska, B. V. K. J. Schmidt, S. Wuttke, *Chem. Soc. Rev.* **2020**, *49*, 3348.
[9] G. Ma, G. Ning, Q. Wei, *Carbon* **2022**, *195*, 328.
[10] S. K. Singh, K. Takeyasu, J. Nakamura, *Adv. Mater.* **2019**, *31*, 1804297.
[11] X. Zhu, C. Hu, R. Amal, L. Dai, X. Lu, *Energy Environ. Sci.* **2020**, *13*, 4536.
[12] L.-L. Ling, L. Jiao, X. Liu, Y. Dong, W. Yang, H. Zhang, B. Ye, J. Chen, H.-L. Jiang, *Adv. Mater.* **2022**, *34*, 2205933.
[13] S. K. Singh, K. Takeyasu, K. Homma, S. Ito, T. Morinaga, Y. Endo, M. Furukawa, T. Mori, H. Ogasawara, J. Nakamura, *Angew. Chem., Int. Ed.* **2022**, *61*, 202212506.
[14] L. Du, L. Xing, G. Zhang, S. Sun, *Carbon* **2020**, *156*, 77.
[15] Y. Shang, X. Xu, B. Gao, S. Wang, X. Duan, *Chem. Soc. Rev.* **2021**, *50*, 5281.
[16] C. Ouyang, L. Zheng, Q. Zhang, X. Wang, *Adv. Mater.* **2022**, *34*, 2205372.
[17] M. Ha, D. Y. Kim, M. Umer, V. Gladkikh, C. W. Myung, K. S. Kim, *Energy Environ. Sci.* **2021**, *14*, 3455.
[18] F. Luo, A. Roy, L. Silvioli, D. A. Cullen, A. Zitolo, M. T. Sougrati, I. C. Oguz, T. Mineva, D. Teschner, S. Wagner, J.u Wen, F. Dionigi, U. I. Kramm, J. Rossmeisl, F. Jaouen, P. Strasser, *Nat. Mater.* **2020**, *19*, 1215.
[19] L. Han, S. Song, M. Liu, S. Yao, Z. Liang, H. Cheng, Z. Ren, W. Liu, R. Lin, G. Qi, X. Liu, Q. Wu, J. Luo, H. L. Xin, *J. Am. Chem. Soc.* **2020**, *142*, 12563.
[20] B. Singh, M. B. Gawande, A. D. Kute, R. S. Varma, P. Fornasiero, P. Mcneice, R. V. Jagadeesh, M. Beller, R. Zboril, *Chem. Rev.* **2021**, *121*, 13620.
[21] G. Vilé, P. Sharma, M. Nachtegaal, F. Tollini, D. Moscatelli, A. Sroka-Bartnicka, O. Tomanec, M. Petr, J. Filip, I. S. Pieta, R. Zboril, M. B. Gawande, *Sol. RRL* **2021**, *5*, 2100176.
[22] S. Li, C. Cheng, A. Thomas, *Adv. Mater.* **2017**, *29*, 1602547.
[23] B. Liu, S. Zhan, J. Du, X. Yang, Y. Zhao, L. Li, J. Wan, Z.-J. Zhao, J. Gong, N. Yang, R. Yu, D. Wang, *Adv. Mater.* **2022**, 2206450.
[24] Y. Manawi, Ihsanullah, A. Samara, T. Al-Ansari, M. Atieh, *Materials* **2018**, *11*, 822.
[25] K. Tewatia, A. Sharma, M. Sharma, A. Kumar, *Mater. Today Proc.* **2021**, *44*, 3933.
[26] B. M. Matsagar, R.-X. Yang, S. Dutta, Y. S. Ok, K. C.-W. Wu, *J. Mater. Chem. A* **2021**, *9*, 3703.
[27] X. Wang, A. Dong, Y. Hu, J. Qian, S. Huang, *Chem. Commun.* **2020**, *56*, 10809.
[28] C. Wang, J. Kim, J. Tang, M. Kim, H. Lim, V. Malgras, J. You, Q. Xu, J. Li, Y. Yamauchi, *Chem* **2020**, *6*, 19.
[29] A. Mehmood, M. Gong, F. Jaouen, A. Roy, A. Zitolo, A. Khan, M.-T. Sougrati, M. Primbs, A. M. Bonastre, D. Fongalland, G. Drazic, P. Strasser, A. Kucernak, *Nat. Catal.* **2022**, *5*, 311.
[30] L. Yan, Y. Xu, P. Chen, S. Zhang, H. Jiang, L. Yang, Y. Wang, L.i Zhang, J. Shen, X. Zhao, L. Wang, *Adv. Mater.* **2020**, *32*, 2003313.
[31] S. San, B. Feng, Z. Xu, J. Yu, Z. Cao, Y. Fan, S. Zhang, *J. Electrochem. Soc.* **2022**, *169*, 106504.
[32] S. Glowniak, B. Szczesniak, J. Choma, M. Jaroniec, *Mater. Today* **2021**, *46*, 109.
[33] Z. Song, L. Zhang, K. Doyle-Davis, X. Fu, J.-L. Luo, X. Sun, *Adv. Energy Mater.* **2020**, *10*, 2001561.
[34] Z. Zhao, Y. Sun, F. Dong, *Nanoscale* **2015**, *7*, 15.
[35] Z. Yang, Z. Yao, G. Li, G. Fang, H. Nie, Z. Liu, X. Zhou, X.i' Chen, S. Huang, *ACS Nano* **2012**, *6*, 205.
[36] Z. Ma, S. Dou, A. Shen, L. Tao, L. Dai, S. Wang, *Angew. Chem., Int. Ed.* **2015**, *54*, 1888.
[37] Y. Li, Y.-S. Hu, H. Li, L. Chen, X. Huang, *J. Mater. Chem. A* **2016**, *4*, 96.
[38] F. Salver-Disma, J.-M. Tarascon, C. Clinard, J.-N. Rouzaud, *Carbon* **1999**, *37*, 1941.
[39] W. Wan, C. A. Triana, J. Lan, J. Li, C. S. Allen, Y. Zhao, M. Iannuzzi, G. R. Patzke, *ACS Nano* **2020**, *14*, 13279.
[40] X. Zhang, Y. Wang, M. Gu, M. Wang, Z. Zhang, W. Pan, Z. Jiang, H. Zheng, M. Lucero, H. Wang, G. E. Sterbinsky, Q. Ma, Y.-G. Wang, Z. Feng, J. Li, H. Dai, Y. Liang, *Nat. Energy* **2020**, *5*, 684.
[41] S. Yang, Y. Yu, X. Gao, Z. Zhang, F. Wang, *Chem. Soc. Rev.* **2021**, *50*, 12985.
[42] W. Wan, Y. Zhao, S. Wei, C. A. Triana, J. Li, A. Arcifa, C. S. Allen, R. Cao, G. R. Patzke, *Nat. Commun.* **2021**, *12*, 5589.
[43] D. Xi, J. Li, J. Low, K. Mao, R. Long, J. Li, Z. Dai, T. Shao, Y. Zhong, Y.u Li, Z. Li, X. J. Loh, L.i Song, E. Ye, Y. Xiong, *Adv. Mater.* **2022**, *34*, 2104090.
[44] A. P. Grosvenor, B. A. Kobe, M. C. Biesinger, N. S. Mcintyre, *Surf. Interface Anal.* **2004**, *36*, 1564.
[45] C. Colomban, E. V. Kudrik, V. Briois, J. C. Shwarbrick, A. B. Sorokin, P. Afanasiev, *Inorg. Chem.* **2014**, *53*, 11517.
[46] J. M. Mccormick, R. C. Reem, E. I. Solomon, *J. Am. Chem. Soc.* **1991**, *113*, 9066.
[47] S. Y. Ha, J. Park, T. Ohta, G. Kwag, S. Kima, *Electrochem. Solid-State Lett.* **1999**, *2*, 461.
[48] P. T. Araujo, M. Terrones, M. S. Dresselhaus, *Mater. Today* **2012**, *15*, 98.
[49] A. C. Ferrari, D. M. Basko, *Nat. Nanotechnol.* **2013**, *8*, 235.
[50] A. Murali, M. Sakar, S. Priya, R. J. Bensingh, M. A. Kader, in *Nanoscale Graphitic Carbon Nitride*, Elsevier, New York **2022**, p. 487.
[51] M. Ahmad, S. R. P. Silva, *Carbon* **2020**, *158*, 24.
[52] Q. Xu, W. Li, L. Ding, W. Yang, H. Xiao, W.-J. Ong, *Nanoscale* **2019**, *11*, 1475.
[53] L. S. Lobo, S. A. C. Carabineiro, *Nanomaterials* **2021**, *11*, 143.
[54] W. Wan, S. Wei, J. Li, C. A. Triana, Y. Zhou, G. R. Patzke, *J. Mater. Chem. A* **2019**, *7*, 15145.
[55] F. Gao, W. Tian, Z. Wang, F. Wang, *Constr. Build. Mater.* **2020**, *260*, 120452.
[56] J. Yang, F. Xiang, H. Guo, L. Wang, X. Niu, *Carbon* **2020**, *156*, 514.
[57] X. Zhang, S. Yao, P. Chen, Y. Wang, D. Lyu, F. Yu, M. Qing, Z. Q. Tian, P. K. Shen, *J. Catal.* **2020**, *389*, 677.
[58] J.-T. Jin, X.-C. Qiao, F.-L. Cheng, H.-B. Fan, L.-F. Cui, *Carbon* **2017**, *122*, 114.